

A model of the earthquake cycle along the Gofar oceanic transform faults

Meng (Matt) Wei ¹, Lingchao He ¹, Bridget Smith-Konter ²

¹Graduate School of Oceanography, University of Rhode Island, ²Department of Earth Sciences, University of Hawaii Manoa

Author contributions: *Conceptualization:* M. Wei, B. Smith-Konter. *Data Curation:* M. Wei, L. He. *Formal Analysis:* M. Wei. *Funding Acquisition:* M. Wei. *Investigation:* M. Wei, L. He, B. Smith-Konter. *Methodology:* B. Smith-Konter. *Software:* B. Smith-Konter. *Visualization:* M. Wei. *Writing – original draft:* M. Wei. *Writing – review and editing:* M. Wei, L. He, B. Smith-Konter.

Abstract The Gofar oceanic transform fault at the East Pacific Rise has one of the best seismic cycles recorded by modern instruments. The timing, location, and magnitude of major earthquakes ($M_w > 5.5$) have been well constrained by data from global seismic networks for the past 30 years. The earthquake interval is short, about 3-5 years. Several segments have already experienced 5 cycles since 1995, when the seismic network was good enough for surface wave relocation. Two ocean bottom seismometer deployments (2008-2009, 2021-2023) also provide constraints on the seismic properties on the fault. This makes Gofar an ideal place to study earthquake cycles. Here, we developed a model for the seismic cycle along the Gofar transform fault using a semi-analytical approach for rapidly calculating 3D time-dependent deformation and stress caused by screw dislocations embedded within an elastic layer overlying a Maxwell viscoelastic half-space. The 160-km long fault is divided into three major segments with six asperities. Our model simulates the earthquake pattern on this fault for the past 30 years. Most of the time, each asperity ruptured as a large earthquake every 3-5 years. Most segments have a nearly constant Coulomb stress threshold of 2-3 MPa, providing optimal conditions for the forecasting of future earthquakes along Gofar. For three cases that deviated from this simple regular pattern, a large earthquake occurred with a centroid location between two asperities. This is likely due to concurrent rupture that involved both asperities. We also modeled surface deformation with different elastic layer thicknesses and mantle viscosities. Even though most deformation is in the horizontal direction, the difference in both horizontal and vertical directions between models can be as large as a few centimeters per year. Several seafloor geodesy methods can be used to differentiate between models, and seafloor pressure might be the most appropriate one at this remote location.

Non-technical summary Large earthquakes repeatedly occur on the same fault over many cycles. Most earthquake cycles are hundreds of years long and therefore difficult to observe. A special kind of fault in the East Pacific Ocean has very short cycles (3-5 years), and we have a very good record of its seismic behavior for the past 30 years. Here we build a numerical model, which can simulate previous earthquakes and forecast future events. The model can also calculate the surface deformation on the seafloor over time. New data can be collected and compared with different model results, and therefore constrain important parameters of the fault.

1 Introduction

The earthquake cycle is a key, yet enigmatic, concept in seismology. For most large earthquakes on plate boundaries, faults are constantly loaded by the movement of the plates, and major earthquakes occur in a quasi-periodic manner (Scholz, 2002). Progress in understanding earthquake cycles is often hindered by the fact that cycles of large earthquakes are much longer than the modern observation history (McGuire, 2008), and it is difficult to fully understand earthquake cycles from observations that capture only a snapshot of the hundreds- to thousands-year cycles of large earthquakes. Paleo-seismic data could cover multiple cycles, but they suffer from large uncertainties regarding earthquake magnitude, timing, and rupture extent (Weldon et al., 2005). Fast-spreading oceanic transform faults (OTFs) are uniquely suited for studying earth-

quake cycles because the intervals between the largest earthquakes are typically less than 15 years due to high offset rates (Boettcher and McGuire, 2009), so it is possible to observe several earthquake cycles on some OTFs with modern instruments (McGuire, 2008; Sykes and Ekström, 2011). Furthermore, the geometry and thermal structure of OTFs are simpler than a continental system (Roland et al., 2010), providing a simpler case to crack the “codes” of earthquake cycles. OTFs also share some fundamental physics with their continental counterparts, so improved understanding will provide insights into the dynamics of continental faults, such as the San Andreas Fault in California and the North Anatolian Fault in Turkey, both of which have generated devastating earthquakes in recent history (Johnson et al., 2023).

The Gofar oceanic transform fault at the East Pacific Rise is one of the best studied sites among all the

Production Editor:
Gareth Funning
Handling Editor:
Yen Joe Tan
Copy & Layout Editor:
Théa Ragon

Signed reviewer(s):
Roland Bürgmann

Received:
May 31, 2024
Accepted:
October 25, 2024
Published:
November 6, 2024

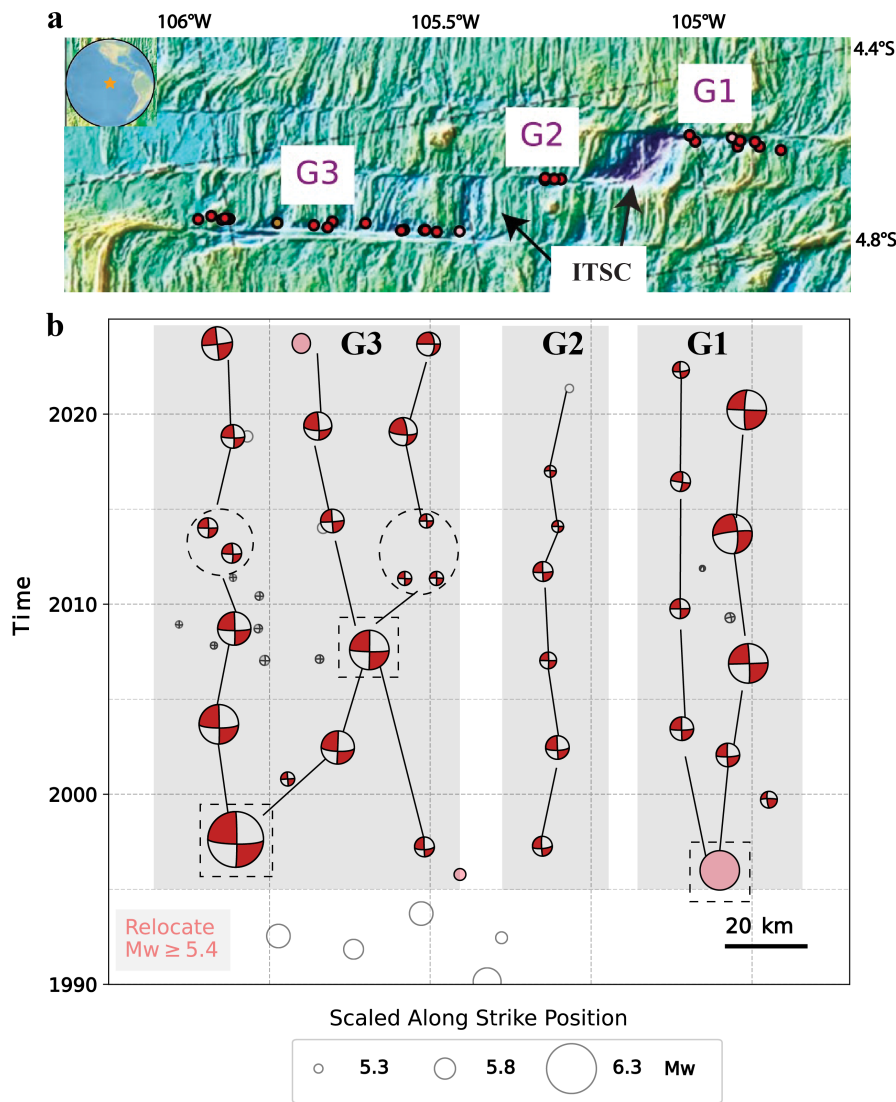


Figure 1 (a) Relocated earthquakes on the Gofar system since 1990. Two intra-transform spreading centers (ITSC) separate the fault into three segments. (b) Time-space plot of the relocated catalog (moment magnitudes from the USGS). Beach balls and filled circles have been relocated with surface waves. Unfilled circles were not relocated due to limited data at that time. The solid lines highlight the earthquakes that ruptured the same segments. The two black dashed circles highlight earthquakes that only ruptured a small part of the seismic segments. The three black dashed squares highlight the earthquakes that might have concurrently ruptured two seismic segments separated by a creeping segment.

oceanic transform faults. The fault is about 160 km long and consists of three major segments (G1, G2, G3) separated by two intra-transform spreading centers (ITSC) (Figure 1). The fault is highly segmented and has an earthquake interval of 3-5 years (McGuire, 2008; Shi et al., 2022; Wolfson-Schwehr et al., 2014). Since 1990, up to six cycles have occurred and been recorded by modern seismic networks. An interesting new observation is that three large earthquakes ($M_w > 5.5$) ruptured the western G3 with a very short time interval (11 days and 18 minutes) in September 2023, suggesting possible synchronization (Lynch et al., 2003; Wei and Shi, 2021; Shi et al., 2022). Moreover, between 2008-2009 and 2021-2023, two field campaigns of ocean bottom seismometers (OBS) were conducted at the fault. In both cases, the OBS array caught a major earthquake ($M_w > 5.5$) on the fault. The 2008-2009 OBS data have been carefully analyzed and constrained many features of the fault sys-

tem (Yao et al., 2011; McGuire et al., 2012; Froment et al., 2014; Guo et al., 2018; Gong and Fan, 2022; Liu et al., 2023). The 2021-2023 data are still being analyzed with publications pending.

The objective of this paper is to develop a simple mechanical model for the earthquake cycle on the Gofar transform fault, which allows us to study the deformation and stress evolution on the fault for the past few earthquake cycles. First, we relocated major earthquakes on the system using surface wave cross-correlation. Next, we used the improved earthquake location data to construct the fault geometry and segmentation (seismic versus creep). Then, we utilized the crustal deformation software package Maxwell to run the simulation and analyzed the results. Lastly, we explored how seafloor geodesy can help distinguish between models and estimate key parameters of the Gofar seismic fault system.

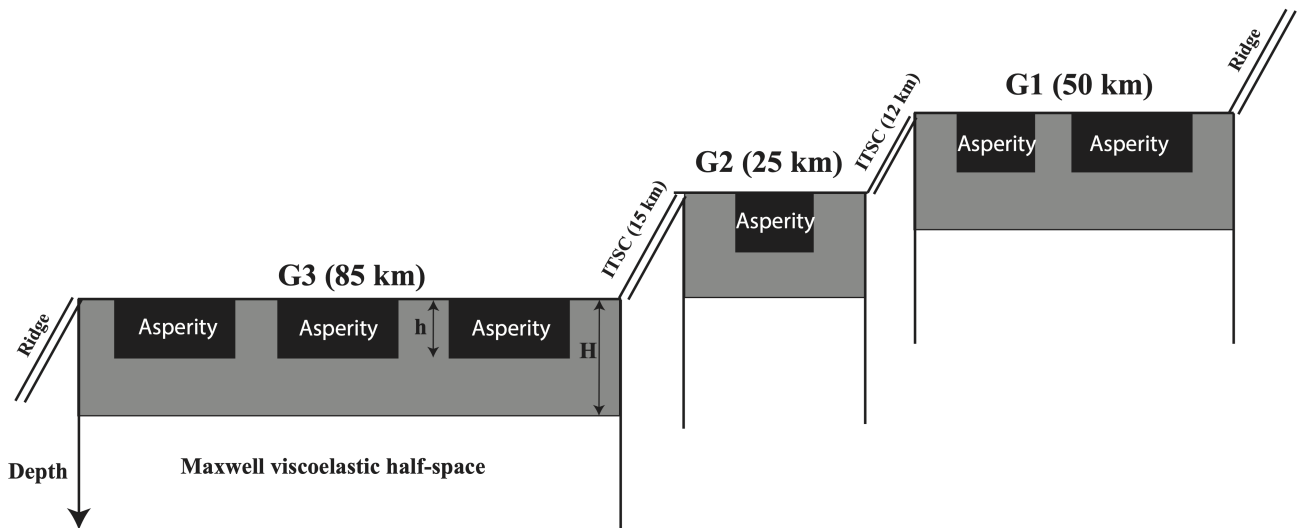


Figure 2 The model setup of the Gofar oceanic transform fault system at the East Pacific Rise. The system consists of three segments separated by two intra-transform spreading centers (ITSCs). The gray and black areas represent the brittle-elastic part of the fault. The black patches are the seismic segments, whose locations and widths are constrained by relocated earthquakes. The gray areas are creeping faults, which only slip aseismically. H is the elastic plate thickness and h is the representative asperity locking depth.

2 Methods

2.1 Earthquake relocation

We used cross-correlation between teleseismic surface waves to relocate OTF earthquakes on Gofar (McGuire, 2008; Cleveland and Ammon, 2015; Howe et al., 2019; Castellanos et al., 2020; Shi et al., 2022; Wolfson-Schwehr et al., 2014). We obtained events from USGS earthquake catalogs between 1 January 1950 and 1 November 2023 (<https://earthquake.usgs.gov/earthquakes/search>). Relocations were performed on events after 1990, with the majority occurring after 1995 when the global seismic network had achieved an adequate distribution for this task. We assumed an R1 Rayleigh wave group velocity of 3.75 km/s (Nishimura and Forsyth, 1988). We used waveform data from the Global Seismic Network (<https://www.iris.edu/hq/programs/gsn>; network code GSN) and GEOSCOPE (<http://geoscope.ipgp.fr/networks/detail/G/>; network code G) because they provide satisfactory azimuthal coverage. Raw waveforms were truncated using a velocity window of 5 km/s to 3 km/s and were bandpass filtered (zero phase) between 0.02 Hz and 0.04 Hz and tapered. Cross-correlation between two events yields several differential times at stations of different azimuths. A cosine fitting from azimuths to differential times gives the relative distance, the azimuth, and their uncertainties between an event pair. Such information was then passed through chains of event pairs to collectively relocate all events in the clusters (Cleveland and Ammon, 2015; Shi et al., 2022). Finally, the cluster was shifted depending on the availability of accurate hydroacoustic catalogs or on the geological features from high-resolution bathymetry data (Pan et al., 2002).

The relocated earthquakes (Figure 1) show that the

Gofar system consists of 6 major seismic segments (3 on G1, 1 on G2 and 2 on G3). The earthquake cycle on these segments is quasi-periodic with an average interval of 3–5 years. Sometimes, a segment ruptures as two smaller earthquakes within a cycle. For example, the western G3 ruptured as two M_w 5.7 in 2012 and 2014, whereas the typical repeater size is M_w 5.9–6.1. Also, three earthquakes appear to be centered on a typical barrier segment (highlighted as dashed squares in Figure 1b). This can be explained by a concurrent rupture of two seismic segments separated by a barrier, which is not uncommon (Philibosian and Meltzner, 2020). More importantly, seismic data indicate that these three earthquakes each had two sub-events separated by several seconds (W. Wu, personal communication), which have been counted as one event in routine analyses.

2.2 Maxwell software and parameters

Maxwell is a crustal deformation software package that uses a semi-analytic approach for rapidly calculating three-dimensional (3D) time-dependent deformation and stress caused by screw dislocations embedded within an elastic layer overlying a Maxwell viscoelastic half-space (Smith and Sandwell, 2004; Sandwell and Smith-Konter, 2018). The Maxwell model was developed in the Fourier domain to exploit the computational advantages of the convolution theorem, hence substantially reducing the computational burden associated with modeling an arbitrarily complex distribution of force couples necessary for fault analysis (Smith and Sandwell, 2003). The software has mostly been used to model the San Andreas Fault System (Smith and Sandwell, 2006; Howell et al., 2016; Ward et al., 2021; Smith-Konter and Sandwell, 2009). A new version of the Maxwell package added the ability to model lateral vari-

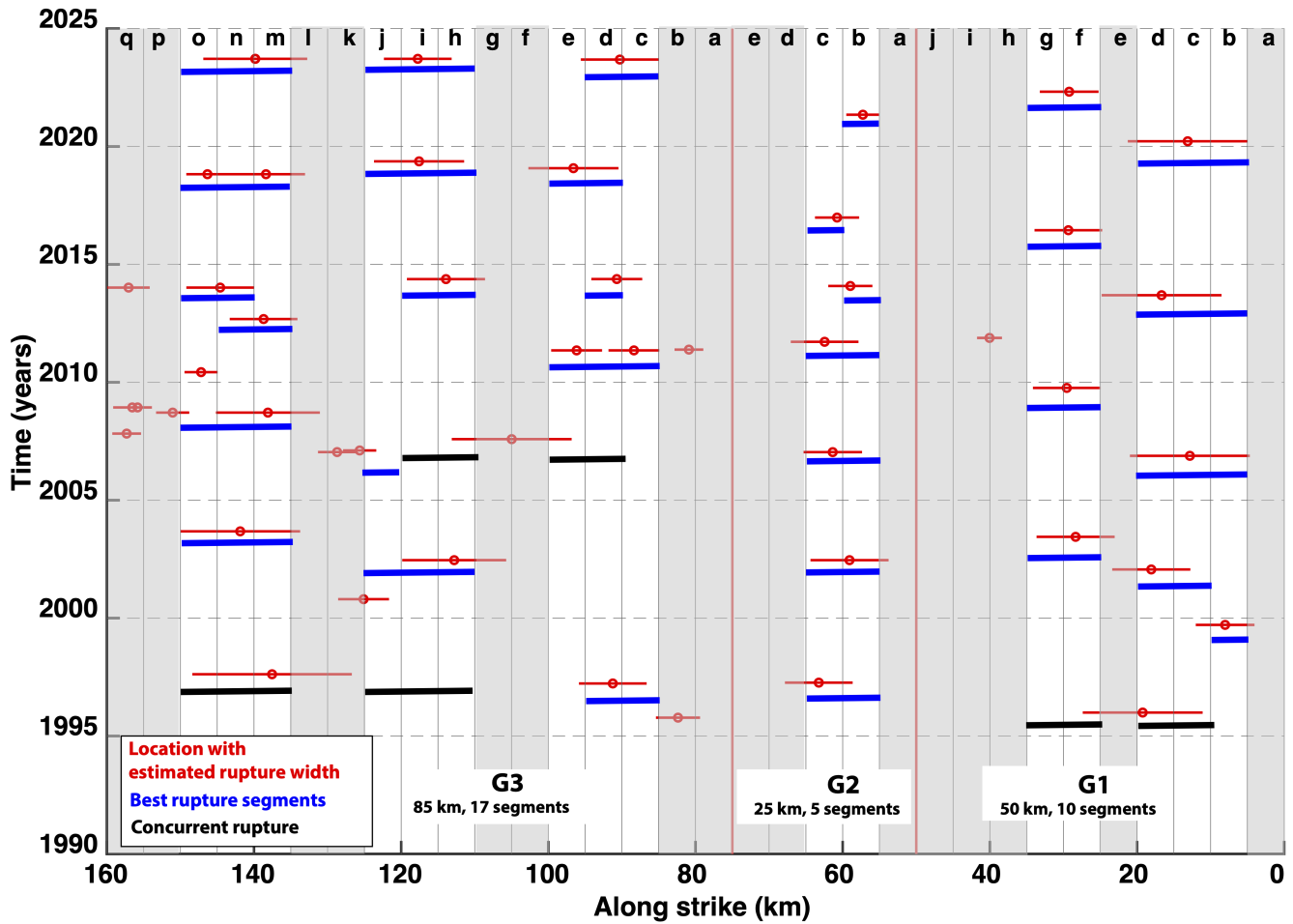


Figure 3 Earthquake history and segmentation on the Gofar transform system. The gray areas are the creeping segments, and the white areas are the asperities. The small red circles represent the relocated centroid locations of the earthquakes, and the horizontal red lines show the estimated rupture lengths at depth, using the empirical equation from Wells and Coppersmith (1994). The blue horizontal lines depict the rupture history used in the modeling. The timing is shifted downwards for easier visualization, but accurate earthquake timing is used in the simulation. The bold black horizontal lines indicate the rupture history in three earthquakes that likely involved concurrent rupture of segments separated by creeping segments (W. Wu, personal communication). The letters on the top are the names of the segments used in this study. For example, segment G1a means segment a at G1.

ations in shear modulus (Sandwell and Smith-Konter, 2018) and has also been applied to the San Andreas Fault System (Ward et al., 2021, 2022) to better understand time-dependent seismic cycles.

In the Maxwell software package, a fault system is modeled as asperities embedded within an elastic layer over a Maxwell viscoelastic half-space (Smith and Sandwell, 2004; Barbot et al., 2017; Kato, 2002). Here, we use the relocated large earthquakes to determine the six major seismic asperities on the Gofar earthquake system (Figure 2). The 160-km long fault system is further divided into thirty-two 5-km long sub-segments with sixteen assigned asperities (Figure 3). The asperities are estimated by comparing rupture lengths and centroid locations of relocated earthquakes (red horizontal line in Figure 3) with the location of the 5-km sub-segments. We assigned a segment as an asperity when it overlaps with a rupture of multiple repeating large earthquakes. We estimated earthquake rupture length at depth using the empirical equation for strike-slip events from

Wells and Coppersmith (1994). Although this method is derived from continental earthquakes, this approach is consistent with the well-recorded 2008 M6.0 earthquake on the Gofar OTF and the 2015 M7.1 earthquake on Charlie-Gibbs OTF (Shi et al., 2022). With this information, we constructed a simplified rupture history of the fault system (Figure 3). During an earthquake, one or more such 5-km segments slip. As discussed earlier, three earthquakes seem to be centered at a barrier segment. We assumed that these earthquakes ruptured two asperities separated by a barrier nearly simultaneously, which is consistent with seismic data (W. Wu, personal communication).

The two-dimensional (2D) map-view domain of the Gofar model space is 1024x1024 pixels, and the grid size is 250 m x 250 m. The Maxwell software places a mirror image of the force couple distribution in a mirror grid so that the net moment is zero and the Fourier transformation can be used (Smith and Sandwell, 2003). The line of symmetry is on the north boundary, parallel to

Symbol	Physics meaning	Value	References
h	The locking depth, above which the seismic segments (asperities in Figure 2) slip during earthquakes and remain locked between earthquakes.	8 km	Yao et al. (2011); McGuire et al. (2012); Froment et al. (2014); Guo et al. (2018); Smith and Sandwell (2006)
μ	Shear modulus of the brittle layer	48 GPa	Roland et al. (2012); Gong and Fan (2022)
H	Elastic plate thickness. The slip between h and H is aseismic.	10, 20, 40 km	Johnson and Segall (2004); Smith and Sandwell (2006); Barnhoorn et al. (2011); Decriem and Árnadóttir (2012); Li et al. (2022)
ν	Viscosity of the mantle	$10^{17}, 10^{18}, 10^{20}$ Pa·s	Pollitz et al. (2001); Johnson and Segall (2004); Smith and Sandwell (2006); Barnhoorn et al. (2011); Decriem and Árnadóttir (2012); Li et al. (2022); Pollitz (2019); Pollitz et al. (2021)

Table 1 Key parameters used in the Gofar simulation.

the fault traces. Consequently, the effective domain becomes 512x1024 pixels, corresponding to dimensions of 128 x 256 km. We experimented with a finer grid size of 125 m and found that the difference in results compared to the 250 m grid size is negligible. For each calculation, we specify an observation depth plane. 3D results can be obtained with repeating calculations at different depths.

We set the boundary condition to best simulate a strike-slip environment that drives the OTFs. The fault parallel boundaries are set to uniform far-field velocity, and the fault perpendicular boundaries have a constant far-field velocity difference across the transform plate boundary and is simulated using a cosine transform in the fault perpendicular direction. This will introduce unrealistic deformation beyond the two ocean ridges, which will be discussed later.

The stress loading rate was estimated using a back-slip method (Savage and Burford, 1973; Smith and Sandwell, 2006). The timing of the earthquakes was derived from the earthquake catalog, and the slip was estimated based on the time elapsed since the last event on that segment.

The key parameters in the model are listed in Table 1. The locking depth and shear modulus were estimated from previous studies at Gofar. The elastic layer thickness and viscosity of the mantle near Gofar are not well constrained, due to the lack of seafloor geodetic measurements, so we tested multiple values within a reasonable range from studies in California and Iceland. Since the structure of oceanic and continental lithosphere is quite different (Fischer et al., 2020), studies from Iceland might be more applicable to Gofar.

We set the locking depth h to 8 km, above which most earthquakes occur in West Gofar (Gong and Fan, 2022). The earthquake depth in East Gofar is not well constrained, but it should not be significantly different from that in West Gofar. While McGuire et al. (2012) observed a much deeper seismicity depth on a barrier patch at West Gofar, Gong and Fan (2022) observed much less depth variation. The discrepancy does not affect our model because we assume the barriers to be creeping,

and thus no locking depth is prescribed at the barrier patch. Smith-Konter et al. (2011) established that on the San Andreas Fault, geodetic locking depths correspond to seismogenic depths identified at the 95% seismicity cutoff, with a close agreement within 2 km for most fault segments. Since no geodetic data are available at Gofar to estimate the locking depth, we assumed a depth of 8 km, which is close to the 95% cutoff depth in seismicity at Gofar (Gong and Fan, 2022).

The shear modulus (μ), also called rigidity, is the product of the density and the square of the shear wave velocity of the elastic layer. Gong and Fan (2022) developed a one-dimensional (1D) shear wave velocity model for Gofar derived from a 2D P-wave travel-time tomographic model (Roland et al., 2012), assuming a constant V_p/V_s ratio of 1.9 in the crust (above 6.85 km depth) and 1.8 in the mantle (below 6.85 km depth). The average shear wave velocity above 20 km depth in this 1D model is about 4 km/s. Assuming an average density of 3.0 g/cm³, the shear modulus of the elastic layer is calculated to be about 48 GPa.

We assessed the sensitivity of the elastic plate thickness at 10, 20, and 40 km. The elastic plate thickness is defined as the elastically strong portion of the lithosphere that is responsible for supporting topographic loads. By studying deformation caused by volcanic loads on the ocean lithosphere, the elastic thickness is, on first order, proportional to the age of the ocean crust (Watts, 1978; Calmant et al., 1990; Watts and Zhong, 2000; Watts and Burov, 2003). This leads to a very small and unrealistic elastic plate thickness of up to 3 km at Gofar. On one hand, the simple relationship between plate thickness and age might be more appropriate for older lithosphere. On the other hand, it has been noticed that geophysical observations sampling geologically long time periods (> 1 Myr) result in a lower estimate of elastic plate thickness than observations of stress relaxation over much shorter times (tens of years) (Smith and Sandwell, 2006; Pollitz, 2019). For example, models based on gravity-topography relations (Lowry et al., 2000), effectively accounting for 1 Myr of loading, yield elastic plate thickness values of 5–15 km in

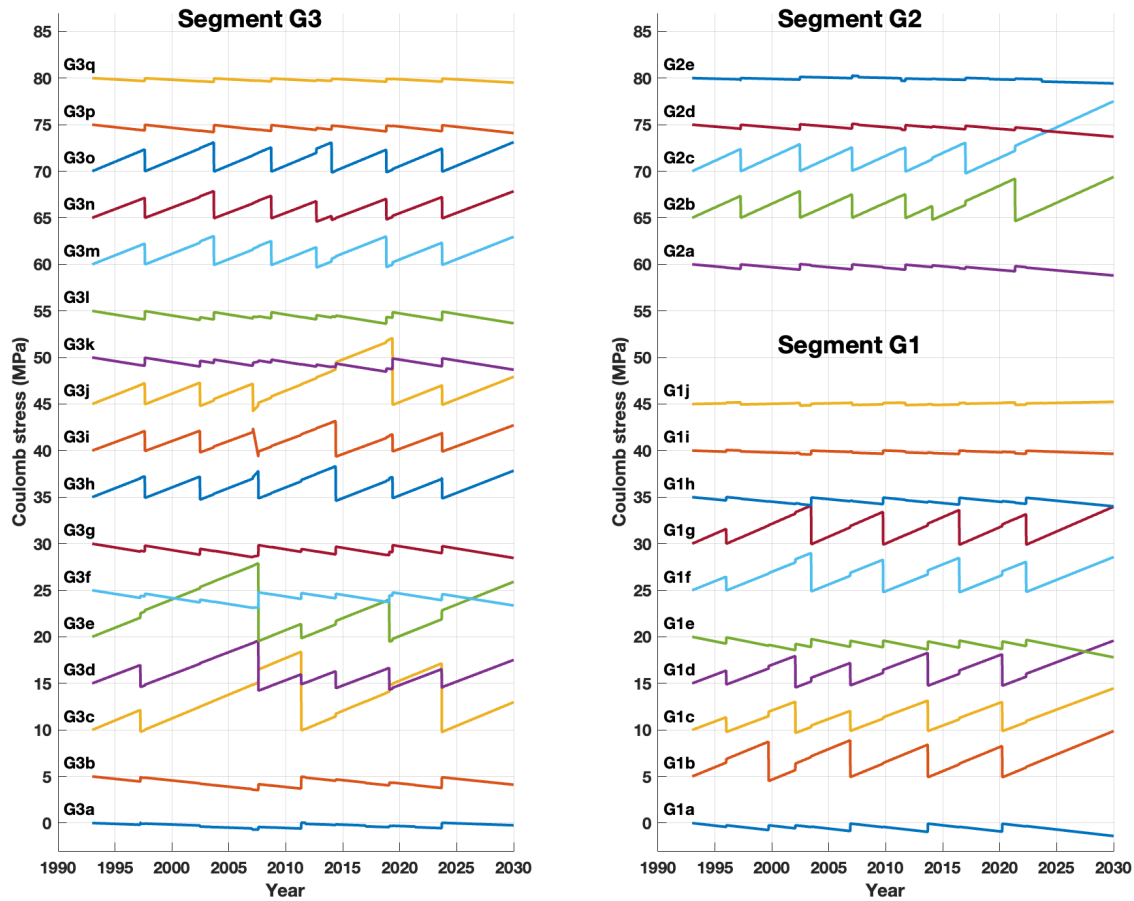


Figure 4 Coulomb stress evolution at 4 km depth in the center of all the segments for a model with elastic plate thickness $H = 40$ km and viscosity $= 10^{20}$ Pa·s. Models with lower viscosity (10^{17} - 10^{19} Pa·s) do not affect the output because the elastic layer is so thick.

the western United States. In contrast, [Johnson and Segall \(2004\)](#) estimate an elastic layer thickness of 40-100 km for central California after studying the post-seismic deformation of the 1906 San Francisco earthquake, while [Smith and Sandwell \(2006\)](#) estimate an elastic layer thickness of more than 60 km in California using GNSS data. Studies in Iceland on deglaciation ([Barnhoorn et al., 2011](#)) reported 27-40 km lithospheric thickness, while post-rifting deformation ([Decriem and Árnadóttir, 2012](#); [Li et al., 2022](#)) generally used 15-20 km elastic layer thickness. Plate thickness affects the amplitude and wavelength of deformation and plays a role in the timescale of observed deformation, particularly in the vertical dimension ([Smith and Sandwell, 2004](#); [Lu et al., 2021](#)). Thick elastic plate models yield larger wavelength postseismic features but shorten the duration of the vertical response compared to thin plate models ([Smith and Sandwell, 2006](#)). Additionally, results from a thick plate model are very similar to those from an elastic half-space model ([Kato, 2002](#)).

Viscosity estimates range from 10^{16} to 10^{21} Pa·s in different studies across various tectonic environments ([Pollitz, 2019](#)). [Pollitz et al. \(2001\)](#) inferred an upper layer viscosity of 4×10^{17} Pa·s to model deformation fol-

lowing the 1999 Hector Mine earthquake in the Mojave Desert. [Johnson and Segall \(2004\)](#) reported 1×10^{19} - 2.9×10^{20} Pa·s for central California with geodetic data constraining the post seismic strain following the 1906 San Francisco earthquake. The 2019 Ridgecrest earthquake sequence contributes to this range with estimates of transient mantle asthenosphere viscosity at approximately 1.3×10^{17} Pa·s, and an adjacent Central Valley transient mantle asthenosphere viscosity of about 7×10^{17} Pa·s ([Pollitz et al., 2021](#)). [Barnhoorn et al. \(2011\)](#) reported 2×10^{18} - 10^{19} Pa·s mantle viscosity by studying the deglaciation cycles in Iceland. [Decriem and Árnadóttir \(2012\)](#) reported an upper mantle viscosity of 1 - 3×10^{18} Pa·s in the South Iceland Seismic Zone observed by geodetic data between 2000-2008. [Li et al. \(2022\)](#) reported mantle viscosity of 0.4×10^{19} Pa·s by studying the post-rifting deformation using geodetic data between 2015-2020. It is not clear which values best apply to Gofar. One unique aspect of the oceanic upper mantle is the potential effect of water-penetrated faults, which can reduce the viscosity by 1-2 order of magnitude ([Hirth and Kohlstedt, 1996](#); [Kohli and Warren, 2020](#); [Kohli et al., 2021](#); [Bürgmann and Dresen, 2008](#)). Therefore, we ran simulations with different viscosities

Segment	The maximum Coulomb stress at the center of the segment at 4 km depth for the past few cycles (MPa)						Average (MPa)	STD (MPa)	Next event time* (Year)	Uncertainty (Year)**
G1b	3.74	3.89	3.42	3.27			3.58	0.28	2027.41	0.15
G1c	3.03	2.04	3.15	3.01			2.81	0.52	2026.37	0.28
G1d	2.94	2.19	3.27	3.13			2.88	0.48	2026.31	0.26
G1f	4	3.28	3.48	3.06			3.45	0.40	2029.76	0.22
G1g	4.1	3.42	3.62	3.16			3.57	0.40	2029.24	0.21
G2b	2.34	2.87	2.52	2.54	1.26	4.2	2.62	0.95	2026.82	0.52
G2c	2.36	2.9	2.57	2.41	3.07		2.66	0.31	2021.36	0.17
G3c	8.4	7.15					7.77	0.88	> 2030	0.45
G3d	1.96	4.58	0.97	1.3	1.66	1.53	2	1.31	2028.89	0.66
G3e	7.91	1.38	4				4.43	3.29	2026.97	1.67
G3h	2.25	2.21	2.78	3.32	2.17	2.04	2.46	0.49	2029.2	0.25
G3i	2.11	2.13	2.34	3.18	1.75	1.91	2.24	0.50	2028.94	0.26
G3j	2.23	2.29	2.18	7.07	2.03		3.16	2.19	> 2030	1.11
G3m	2.23	3.04	2.51	1.84	3.01	2.33	2.49	0.47	2029.02	0.24
G3n	2.14	2.86	2.37	1.78	2.03	2.23	2.24	0.37	2028.69	0.19
G3o	2.34	3.1	2.56	3.09	2.31	2.44	2.64	0.36	2029.04	0.18

Table 2 The Coulomb stress threshold at 4 km depth and the predicted time for the next event for each fault segment.

*The predicted time is based on the average maximum Coulomb stress on the segment at 4 km depth.

**The uncertainty is based on the standard deviation (STD) of the maximum Coulomb stress at the center of the segment at 4 km depth for the past few cycles.

($10^{17} - 10^{20}$ Pa·s) and compared these results.

3 Results

3.1 Coulomb stress evolution

Coulomb stress (σ_f) can be used to evaluate a fault's stressing behavior throughout the earthquake cycle. In this study, we calculate Coulomb stress accumulation at seismogenic depths as $\sigma_f = \tau - \mu_f \sigma_n$, where τ is the shear stress, μ_f is the effective coefficient of friction, and σ_n is the effective normal stress. Because stress varies as a function of observation depth within the seismogenic zone, we calculate the representative stress at 4 km depth, which is 1/2 of the local locking depth, following King et al. (1994). Stress calculations are performed on a fault-segment by fault-segment basis, thus only the local fault contributes to the final stress result. Restraining bends have higher normal stress and lower rates of Coulomb stress accumulation; releasing bends have lower normal stress and higher rates of Coulomb stress accumulation. For the Gofar system, the largest angular deviation of a local strike-slip segment from the average slip direction is very small, thus the normal stress contribution to the total Coulomb stress calculation is generally less than 10%. Therefore, the exact value of the effective coefficient of friction is not a crucial parameter. Here, we set μ_f to be 0.6.

We began our analysis with a very thick ($H = 40$ km)

elastic plate model, which closely resembles a pure elastic half-space model (Kato, 2002). The Coulomb stress evolution at 4 km depth in the center of all the segments for a model with 10^{20} Pa·s viscosity is shown in Figure 4. Lowering the viscosity (10^{17} - 10^{19} Pa·s) does not affect the output because the elastic layer is so thick. Coulomb stress on the seismic asperities increases linearly between earthquakes and then drops to near zero during earthquakes.

According to this model, most segments have a nearly constant Coulomb stress threshold of 2-3 MPa (Table 2), which reflects the regular and simple repeating earthquake history. The exceptions are G3j and G3c-e, which are caused by a relatively complex rupture history in these segments. According to this model, we can estimate stress thresholds for the next large earthquakes on these segments and forecast future events using these thresholds (Table 2). For segments with regular cycles, the forecasted rupture times are closely aligned for adjacent segments. For example, segments G1f and G1g are estimated to rupture sometime in 2029. Segment G3m, G3n, and G3o are expected to rupture near the end of 2028, where the forecasts are anticipated to be quite good with uncertainty less than three months (Table 2). However, for segments with a complex rupture history, the forecasts can vary significantly for adjacent segments. For instance, segment G2c was estimated to rupture in 2022, but it did not occur. We expect the next earthquake in G2b and G2c will be larger than previous

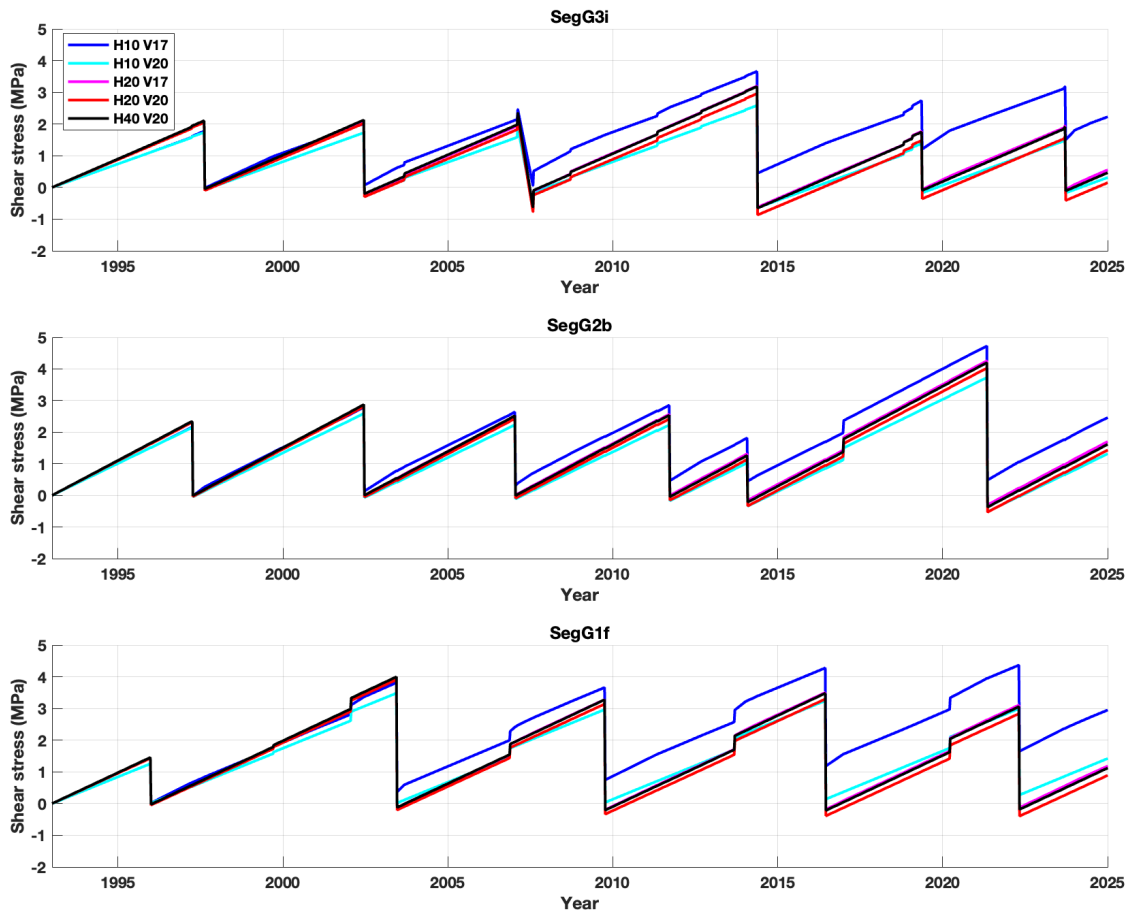


Figure 5 Coulomb stress evolution at 4 km depth in the center of selected segments (G3i, G2b, and G1f) for different H and viscosity. ‘H10 V17’ refers to H = 10 km and viscosity = 10^{17} Pa·s.

ones.

One important question regarding the seismic cycle is why ruptures deviate from a simple repeating pattern in some cases. As discussed earlier, three earthquakes seemed to rupture multiple segments separated by a barrier patch. Our model provides a possible explanation. For the 2007 M6.1 earthquake in G3, our model shows that the Coulomb stress on G3d and G3e was very large at the time of the earthquake. One possible scenario is that the rupture that initiated in G3d and G3e was very large, and it propagated through the barrier patch and triggered slip on G3h and G3i. The two other earthquakes of this kind occurred near the beginning of our simulation; thus we cannot provide any insight. It is possible that these earthquakes also started in a segment that had accumulated an above-normal amount of seismic moment.

Our model could not explain the two cases where no large earthquake occurred during a cycle (G3c-e, G3m-o, 2010-2015). The lack of a large earthquake in G3c-e could be caused by the unusually large rupture in the previous cycle of 2007. This large rupture produced a heterogeneous stress field that could not sustain another large event. Between 2010-2015, G3m-o ruptured as two smaller events, despite the normal size of the pre-

vious rupture. Therefore, this kind of behavior could occur randomly due to the heterogeneous nature of faults (Kato, 2020; Cox et al., 2021).

For a viscoelastic model with a thinner elastic layer (H = 10 or 20 km), the stress evolution is very similar to that of the thick elastic model (H=40 km) but with some noticeable differences (Figure 5). First, the stress loading rate of models with H=10 km is smaller than that of models with a thicker elastic layer, as expected. Second, the effect of the viscoelastic layer becomes noticeable for the thin elastic layer model (H = 10 km) with low viscosity (10^{17} Pa·s). The stressing rate increases due to the viscoelastic effect (Lambert and Barbot, 2016). Because the estimated slip remains the same, the shear stress exhibits an upward trend in the simulation. Modifying the code to adjust the estimated slip based on the shear stress state of the fault segment can eliminate this artificial trend. The stress evolution will be similar to the thick elastic layer model but with a slightly increased stress threshold.

3.2 Surface deformation simulation

We used the same models to estimate surface deformation. First, we estimated the long-term surface velocity without adding deformation caused by earthquakes.

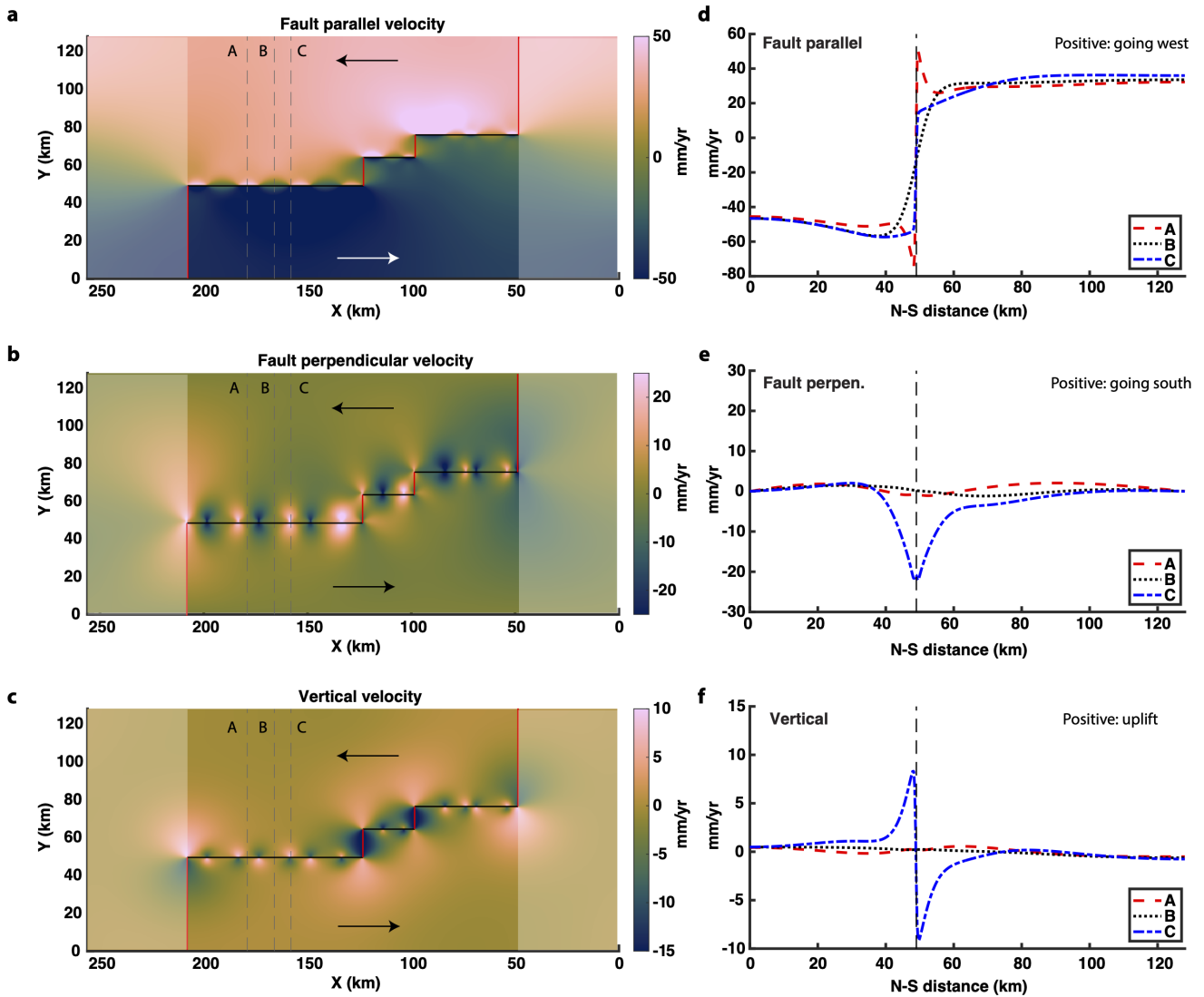


Figure 6 Long-term surface velocity for a model with $H=40$ km and a viscosity of 10^{20} Pa.s. (a) Velocity in the fault parallel direction, with positive indicating westward movement. The black solid lines are the fault trace, and the red lines are spreading centers and ocean ridges. The lightly shaded areas on the sides are regions with unrealistic velocity (see Discussions for details). (b) Velocity in the fault perpendicular direction, with positive indicating southward movement. (c) Velocity in the vertical direction, with positive indicating uplift. (d-f) Velocity profiles for A, B, and C (dashed line in (a-c)) in three directions. Profile A goes through a creeping segment (G3k and G3l). Profile B goes through the center of an asperity segment (G3i). Profile C goes through the boundary between a creeping segment (G3f) and an asperity (G3e).

Second, we incorporated earthquake history into the simulation. Co-seismic deformation is similar across different models. The main difference lies in the post-seismic viscoelastic deformation response. Models with a thin elastic layer and low viscosity exhibit larger post-seismic deformation.

The 3-D long-term surface velocity for a model with $H=40$ km is shown in Figure 6. Because we assume full relaxation, viscosity does not affect the result. The surface velocity varies spatially in all three directions. Surface velocity in the fault-parallel direction is the largest and looks like a step function across the fault trace. The velocity ranges from -60 mm/yr to 40 mm/yr (with positive values indicating movement to the west). Near the fault trace, the velocity difference across the fault varies between 0 and 140 mm/yr depending on whether the segment is creeping or locked between earthquakes.

The velocity in the fault perpendicular direction located near the end of the asperities ranges from 30 mm/yr to -20 mm/yr (positive means going south). The vertical velocity exhibits short-wavelength lobate patterns at the endpoints of locked fault segments, consistent with previous studies (Ward et al., 2022; Smith-Konter et al., 2014), and resulting from double force-couples. Vertical velocities at Gofar range from 10 mm/yr to -10 mm/yr (positive is uplift) near the fault line and decreases to zero when moving away from the fault. Figure 7 shows the comparison of interseismic surface velocity for $H=10, 20,$ and 40 km. The basic features are very similar. However, the fault parallel component is noticeably smaller in the far-field for thinner models, even though at large enough distances, the fault-parallel long-term rates will reach plate rate. The vertical velocity is much higher in the far-field for thinner models, and the fault

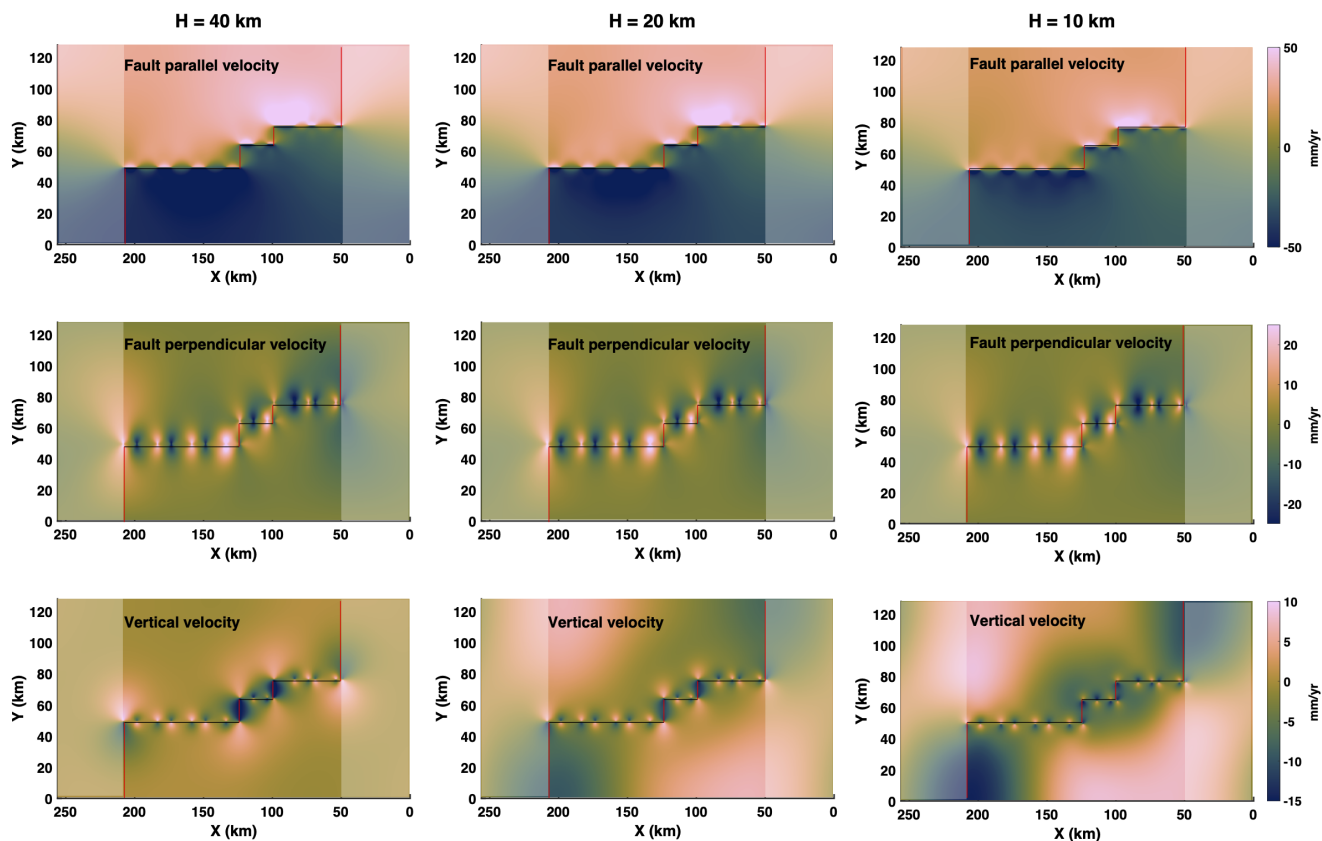


Figure 7 Comparison of long-term surface velocity between models with different elastic layer thicknesses ($H = 10, 20,$ and 40 km). The results shown here all have viscosity of 10^{20} Pa·s but viscosity does not affect the results. The notation for positive directions, lines, and shaded areas are the same as in Figure 6.

perpendicular velocity does not change much with H .

Both elastic layer thickness and viscosity affect the postseismic deformation on the seafloor. We ran simulations beginning in August 2018 (year 2018.8) and calculated the surface deformation until year 2025. These models include long-term velocity, co-seismic, and postseismic deformation. The most significant earthquakes are in 2023 on the western segments (G3). Figure 8A shows the difference in deformation during the year 2025 for two extreme models (H10 V17 and H40 V20). The difference in the fault parallel and vertical directions are more than 70 mm, whereas in the fault perpendicular direction it is 30 mm. Figure 8B shows the displacement history at three locations. The most obvious differences between models are caused by the long-term velocity, which depends on the elastic layer thickness. Thinner models ($H=10$ km) show lower velocity in the fault parallel and fault perpendicular directions but higher velocities in the vertical direction at almost all three locations. For models with the same elastic layer thickness but different viscosities, the models with lower viscosity produce more postseismic deformation. Among the three locations, the most significant difference in deformation between the two extreme models (H10 V17 and H40 V20) in the fault parallel direction is at P1 (> 100 mm). The most extreme difference in the vertical direction is at P2 (~ 60 mm), and that in the fault perpendicular direction is P3 (~ 30 mm).

4 Discussion

4.1 Model simplification

In our model, we simplified the behavior of barrier patches to free creep. However, the actual behavior on faults is much more complex (Wolfson-Schwehr and Boettcher, 2019). This complexity is controlled by heterogeneity in the rheological evolution, which is caused by heterogeneous petrological fabric. This, in turn, is influenced by heterogeneous fracturing, permeability, and fluid flow (Cox et al., 2021; Gregory et al., 2021). Earthquake swarms and foreshocks have been observed at a barrier patch before the 2008 M6.0 earthquake on G3 (McGuire et al., 2012) and might be driven by slow slip events (Liu et al., 2020). Repeating earthquake swarms have also been observed near the western edge of G3 and the eastern edge of G1. These might be driven by magma intrusion activities and/or aseismic slip along the fault (Gong et al., 2023). In both cases, the majority of the energy is released as aseismic slip. The existence of small earthquakes does not significantly affect the major earthquake cycles. The 2008 M6.0 earthquake on G3 might have been triggered by a slow slip event (McGuire et al., 2012; Liu et al., 2020). The slow slip events might have short term influence on the timing of large earthquakes but do not affect the general behavior of the earthquake cycles.

Gong and Fan (2022) proposed a conceptual model of microseismicity and fault slip modes at the western-

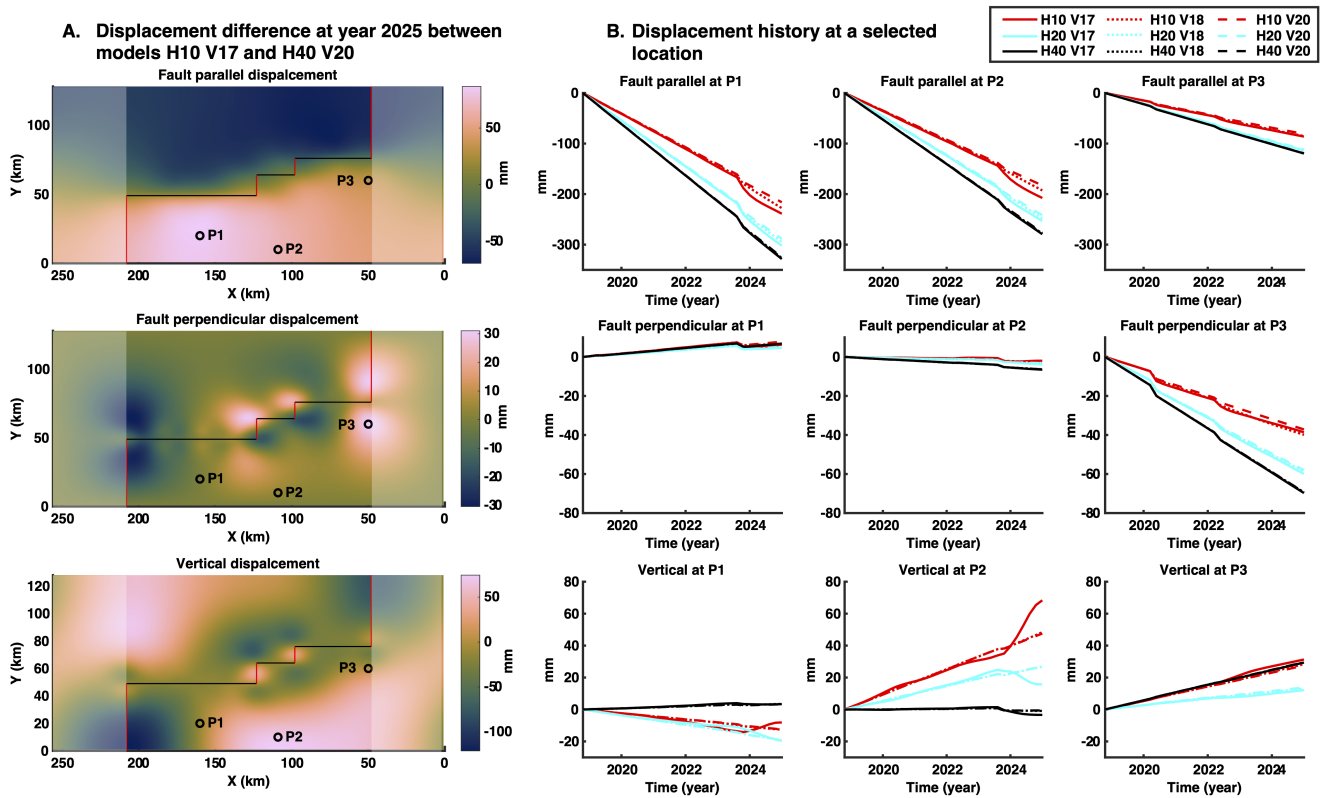


Figure 8 Surface deformation for different models starting in August 2018 (year 2018.8). (A) The displacement difference in year 2025 between model H10 V17 and H40 V20. The three circles are locations of displacement history as shown in (B). The notation for positive directions, lines, and shaded areas are the same as in Figure 6. (B) Displacement history in three directions at three locations. Results from nine models are plotted.

most Gofar transform fault (Figure 10 in Gong and Fan, 2022). In general, their conceptual model is consistent with the asperity model that we proposed for Gofar (Figure 2), where locked patches are separated by barriers with earthquake swarms and slow slip events. However, their model has more details regarding along-strike depth variation and seismicity in the mantle. Also, they only proposed two seismic patches on G3 (zones 3 and 1 in Gong and Fan, 2022) instead of three as simulated here. This difference might be caused by different dataset used: we used global seismic data spanning the past 30 years, while Gong and Fan (2022) mostly relied on OBS data between 2008-2009 when the west segments were mostly active. Future data and events should be able to indicate which one is more likely correct.

We assumed that the brittle crust is elastic in the entire domain, underlain by a viscoelastic medium. While this assumption is adequate for assessing the mechanical response of locked fault segments within Gofar, it is probably not valid at the ocean ridges (the two long vertical red lines at the ends of the fault trace in Figure 6-8), where shallow magma chambers exist (Detrick et al., 1987) and make the crust warmer and more viscous. Hence, our model likely overestimates the surface deformation on the ridge. Furthermore, it is known that some OTFs are under compression or extension (Pockalny, 1997). Our calculations do not include the stress accumulation due to compression or extension beneath

the locked portions of each fault segment because there is little data to constrain that.

In the real OTFs environment, the two fault perpendicular boundaries should also have uniform velocities due to the existence of ocean ridges. Our model does not include ocean ridges, and we focus on OTFs behaviors. Even though the results beyond the two ridges (lightly shaded areas in Figure 6-8) are not realistic, the calculation on the OTFs between the two ridges should be good.

4.2 Coulomb stress threshold

Our model shows that most segments on Gofar have a nearly constant Coulomb stress threshold of 2-3 MPa at 4 km depth (Table 2). This threshold is comparable to modeling studies of other fault systems such as the San Andreas Fault (Smith-Konter and Sandwell, 2009), the North Anatolian Fault (Stein et al., 1997), the Xianshuihe-Xiaojiang Fault (Shan et al., 2013) and the Central Apennines extensional system (Mildon et al., 2019). This threshold is also in agreement with stress drop that was estimated from the spectral analysis of seismograms for moderate to large earthquakes (Allmann and Shearer, 2009). Even though stress drop estimates for individual earthquakes range from about 0.3 to 50 MPa, the median stress drop is about 4 MPa and does not vary with moment between Mw from 5.2 to 8.3 (Allmann and Shearer, 2009). The 2-3 MPa threshold that we observed is evaluated at 4 km depth, and we note that this value varies with depth strongly for

shallower and deeper portions of the asperities. While the average Coulomb stress for the asperities, which is physically equivalent to stress drop, might be half of the value, this is still within the range observed by [Allmann and Shearer \(2009\)](#) and close to the average. Therefore, both numerical models and observations indicate that the Coulomb stress change over earthquake cycles is on the order of a few MPa, regardless of the absolute stress level on these faults.

4.3 Time- and slip-predictable models

Time-predictable model ([Shimazaki and Nakata, 1980](#)) and slip-predictable model ([Bufe et al., 1977](#)) are two popular earthquake cycle models. In the time-predictable model, earthquake will occur once the stress reaches a threshold. Therefore, the timing of the earthquakes is predictable by tracking the stress evolution. In the slip-predictable model, the timing of events is not predictable, but the slip is. The slip is large if the time from the last event is long. Researchers have tested these two models against various datasets and the applicability of these two models are still under debate (see [Rubinstein et al., 2012](#)).

Our model assumes that the slip of an earthquake on a segment is proportional to the time from the last event, which makes our model intrinsically slip-predictable. The evolution of Coulomb stress as shown in Figure 4 is very similar to the classic slip-predictable model. However, because the variation in interval and maximum Coulomb stress is quite small in most asperities, one can estimate the time of the next event using a Coulomb stress threshold (Table 2). Effectively, the earthquake cycle is time predictable with a reasonably small uncertainty at Gofar.

4.4 Seafloor geodesy

Seafloor geodesy has improved significantly over the last several decades ([Bürgmann and Chadwell, 2014](#)) and could be applied at Gofar in the near future. Most surface deformation at Gofar is in the fault-parallel direction. The GNSS-A method can measure horizontal deformation within a few centimeters of uncertainty ([Chadwell and Sweeney, 2010](#); [DeSanto et al., 2023](#)) and seems to offer the best chance of recording tectonic deformation at Gofar. However, the GNSS-A method usually requires three transponders at one location, and measurements can only be made using a surface vehicle (such as a ship or waveglider) in a campaign-style manner. At best, one can get a couple of measurements per year. The remote location of Gofar has limited the practical use of the GNSS-A method. However, as technology advances, this situation might change. For example, a mooring-based surface platform could be deployed to collect data more continuously. Even a few measurements over a few years could be useful to distinguish models because the expected difference is quite large. Moreover, oceanic transform faults closer to land, such as Blanco and Mendocino, could be better targets for GNSS-A field projects due to easy access.

In contrast, direct acoustic ranging has been used to measure tectonic deformation across transform faults

in the ocean ([McGuire and Collins, 2013](#); [Lange et al., 2019](#); [Yamamoto et al., 2019](#)). This technique is effective for accessing the locking state of segments and capturing shallow afterslip and slow slip events. However, it can only measure distance between transponders, which is usually only a few kilometers due to the downward bending nature of acoustic wave propagation near the ocean bottom. It is less useful to measure deformation off the fault and has no sensitivity to broader deformation related to mantle rheology.

Another promising tool is seafloor pressure sensors, which can continuously measure vertical seafloor deformation with a couple of centimeters of uncertainty over a five-year period ([Dobashi and Inazu, 2021](#); [Watts et al., 2021](#)). These sensors could be useful at Gofar if deployed at carefully selected locations. For example, P2 in Figure 8 has large difference in vertical motion between models, making it a good potential location for deploying a pressure sensor. Although the measurements are subject to ocean noise due to non-tidal oceanic processes, recent studies have developed methods to reduce this noise to only a few millimeters by removing common ocean signals using a reference station ([Fredrickson et al., 2019, 2023](#)). Further work is necessary to understand the feasibility of implementing pressure sensors at Gofar, including the effects of topographical features and locations with varying water depths.

Given the rapid development of seafloor geodesy in the past few years, it is reasonable to expect future field work at Gofar or other oceanic transform fault systems to collect both seafloor geodesy data and seismic data. Future seafloor geodetic data can be used to illuminate critical characteristics of the fault system and help differentiate between models with different viscosities or locking depths.

5 Conclusions

We developed a numerical model of the earthquake cycle along the Gofar oceanic transform fault system. The 160-km-long fault is divided into three major segments with six asperities. Our model can simulate the earthquake pattern on this fault for the past 30 years. Most of the time, each asperity ruptured as a large earthquake every 3-5 years. Most segments have a nearly constant Coulomb stress threshold of 2-3 MPa, and future earthquakes have been forecasted accordingly. For three cases that deviated from this simple regular pattern, a large earthquake occurred with a centroid location between two asperities. This is likely due to concurrent rupture that involved both asperities. We also modeled surface deformation with different elastic layer thicknesses and mantle viscosities. Even though most deformation is in the horizontal direction, the difference in both horizontal and vertical directions between models can be as large as a few centimeters per year. Advances in seafloor geodesy methods can be used to differentiate between models, and seafloor pressure might be the most appropriate one at this remote location.

Acknowledgements

This research is supported by the U.S. National Science Foundation (Grant 1654416). We thank Roland Burgmann and an anonymous reviewer for their constructive review. We thank Rachel Abercrombie, David Sandwell, Belle Philibosian, and Wenbo Wu for their helpful discussions. For seismic data retrieval and preprocessing for relocation, we utilized ObsPy (<https://doi.org/10.5281/zenodo.3921997>), and for map-related plotting, we used GMT (Wessel et al., 2019) along with Cartopy (<https://scitools.org.uk/cartopy/docs/latest/>). Bathymetry data were obtained from the Global Multi-Resolution Topography data synthesis (Ryan et al., 2009).

6 Data and code availability

The software package Maxwell is available at <https://github.com/dsandwell/fftfault>. The relocated earthquake catalog can be found at <https://doi.org/10.5281/zenodo.11399011>.

7 Competing interests

The authors have no competing interests.

References

- Allmann, B. P. and Shearer, P. M. Global variations of stress drop for moderate to large earthquakes. *Journal of Geophysical Research: Solid Earth*, 114(B1), Jan. 2009. doi: 10.1029/2008jb005821.
- Barbot, S., Moore, J. D. P., and Lambert, V. Displacement and Stress Associated with Distributed Anelastic Deformation in a Half-Space. *Bulletin of the Seismological Society of America*, 107(2):821–855, Mar. 2017. doi: 10.1785/0120160237.
- Barnhoorn, A., van der Wal, W., and Drury, M. R. Upper mantle viscosity and lithospheric thickness under Iceland. *Journal of Geodynamics*, 52(3–4):260–270, Oct. 2011. doi: 10.1016/j.jog.2011.01.002.
- Boettcher, M. S. and McGuire, J. J. Scaling relations for seismic cycles on mid-ocean ridge transform faults. *Geophysical Research Letters*, 36(21), Nov. 2009. doi: 10.1029/2009gl040115.
- Bufe, C. G., Harsh, P. W., and Burford, R. O. Steady-state seismic slip – A precise recurrence model. *Geophysical Research Letters*, 4(2):91–94, Feb. 1977. doi: 10.1029/gl004i002p00091.
- Bürgmann, R. and Chadwell, D. Seafloor Geodesy. *Annual Review of Earth and Planetary Sciences*, 42(1):509–534, May 2014. doi: 10.1146/annurev-earth-060313-054953.
- Bürgmann, R. and Dresen, G. Rheology of the Lower Crust and Upper Mantle: Evidence from Rock Mechanics, Geodesy, and Field Observations. *Annual Review of Earth and Planetary Sciences*, 36(1):531–567, May 2008. doi: 10.1146/annurev-earth.36.031207.124326.
- Calmant, S., Francheteau, J., and Cazenave, A. Elastic Layer Thickening With Age of the Oceanic Lithosphere: A Tool For Prediction of the Age of Volcanoes Or Oceanic Crust. *Geophysical Journal International*, 100(1):59–67, Jan. 1990. doi: 10.1111/j.1365-246x.1990.tb04567.x.
- Castellanos, J. C., Zhan, Z., and Wu, W. Absolute Centroid Location of Submarine Earthquakes from 3D Waveform Modeling of Water Reverberations. *Journal of Geophysical Research: Solid Earth*, 125(5), May 2020. doi: 10.1029/2019jb018941.
- Chadwell, C. D. and Sweeney, A. D. Acoustic Ray-Trace Equations for Seafloor Geodesy. *Marine Geodesy*, 33(2–3):164–186, July 2010. doi: 10.1080/01490419.2010.492283.
- Cleveland, K. M. and Ammon, C. J. Precise Relative Earthquake Magnitudes from Cross Correlation. *Bulletin of the Seismological Society of America*, 105(3):1792–1796, Apr. 2015. doi: 10.1785/0120140329.
- Cox, S., Fagereng, A., and MacLeod, C. J. Shear Zone Development in Serpentinized Mantle: Implications for the Strength of Oceanic Transform Faults. *Journal of Geophysical Research: Solid Earth*, 126(5), May 2021. doi: 10.1029/2020jb020763.
- Decriem, J. and Árnadóttir, T. Transient crustal deformation in the South Iceland Seismic Zone observed by GPS and InSAR during 2000–2008. *Tectonophysics*, 581:6–18, Dec. 2012. doi: 10.1016/j.tecto.2011.09.028.
- DeSanto, J. B., Webb, S. C., Nooner, S. L., Schmidt, D. A., Crowell, B. W., Brooks, B. A., Ericksen, T. L., and Chadwell, C. D. Limited shallow slip for the 2020 Simeonof earthquake, Alaska, constrained by GNSS-Acoustic. *Geophysical Research Letters*, 50(16), Aug. 2023. doi: 10.1029/2023gl105045.
- Detrick, R. S., Buhl, P., Vera, E., Mutter, J., Orcutt, J., Madsen, J., and Brocher, T. Multi-channel seismic imaging of a crustal magma chamber along the East Pacific Rise. *Nature*, 326(6108):35–41, Mar. 1987. doi: 10.1038/326035a0.
- Dobashi, Y. and Inazu, D. Improving Detectability of Seafloor Deformation From Bottom Pressure Observations Using Numerical Ocean Models. *Frontiers in Earth Science*, 8, Jan. 2021. doi: 10.3389/feart.2020.598270.
- Fischer, K. M., Rychert, C. A., Dalton, C. A., Miller, M. S., Beghein, C., and Schutt, D. L. A comparison of oceanic and continental mantle lithosphere. *Physics of the Earth and Planetary Interiors*, 309:106600, Dec. 2020. doi: 10.1016/j.pepi.2020.106600.
- Fredrickson, E. K., Wilcock, W. S. D., Schmidt, D. A., MacCready, P., Roland, E., Kurapov, A. L., Zumberge, M. A., and Sasagawa, G. S. Optimizing Sensor Configurations for the Detection of Slow-Slip Earthquakes in Seafloor Pressure Records, Using the Cascadia Subduction Zone as a Case Study. *Journal of Geophysical Research: Solid Earth*, 124(12):13504–13531, Dec. 2019. doi: 10.1029/2019jb018053.
- Fredrickson, E. K., Gomberg, J. S., Wilcock, W. S. D., Hautala, S. L., Hermann, A. J., and Johnson, H. P. Slow Slip Detectability in Seafloor Pressure Records Offshore Alaska. *Journal of Geophysical Research: Solid Earth*, 128(2), Feb. 2023. doi: 10.1029/2022jb024767.
- Froment, B., McGuire, J. J., van der Hilst, R. D., Gouédard, P., Roland, E. C., Zhang, H., and Collins, J. A. Imaging along-strike variations in mechanical properties of the Gofar transform fault, East Pacific Rise. *Journal of Geophysical Research: Solid Earth*, 119(9):7175–7194, Sept. 2014. doi: 10.1002/2014jb011270.
- Gong, J. and Fan, W. Seismicity, Fault Architecture, and Slip Mode of the Westernmost Gofar Transform Fault. *Journal of Geophysical Research: Solid Earth*, 127(11), Nov. 2022. doi: 10.1029/2022jb024918.
- Gong, J., Fan, W., Boettcher, M., McGuire, J., Warren, J., Behn, M., Roland, E., and Liu, Y. Ridge-transform fault interaction controls earthquake swarm activity at the Gofar transform fault. *AGU Fall Meeting Abstracts*, 2023(39):13–039, 2023.
- Gregory, E. P., Singh, S. C., Marjanović, M., and Wang, Z. Serpentinized peridotite versus thick mafic crust at the Romanche oceanic transform fault. *Geology*, 49(9):1132–1136, June 2021. doi: 10.1130/g49097.1.

- Guo, H., Zhang, H., and Froment, B. Structural control on earthquake behaviors revealed by high-resolution Vp/Vs imaging along the Gofar transform fault, East Pacific Rise. *Earth and Planetary Science Letters*, 499:243–255, Oct. 2018. doi: 10.1016/j.epsl.2018.07.037.
- Hirth, G. and Kohlstedt, D. L. Water in the oceanic upper mantle: implications for rheology, melt extraction and the evolution of the lithosphere. *Earth and Planetary Science Letters*, 144(1–2): 93–108, Oct. 1996. doi: 10.1016/0012-821x(96)00154-9.
- Howe, M., Ekström, G., and Nettles, M. Improving relative earthquake locations using surface-wave source corrections. *Geophysical Journal International*, 219(1):297–312, June 2019. doi: 10.1093/gji/ggz291.
- Howell, S., Smith-Konter, B., Frazer, N., Tong, X., and Sandwell, D. The vertical fingerprint of earthquake cycle loading in southern California. *Nature Geoscience*, 9(8):611–614, June 2016. doi: 10.1038/ngeo2741.
- Johnson, K., Villani, M., Bayliss, K., Brooks, C., Chandrasekhar, S., Chartier, T., Chen, Y.-S., Garcia-Pelaez, J., Gee, R., Styron, R., Rood, A., Simionato, M., and Pagani, M. Global Earthquake Model (GEM) Seismic Hazard Map, 2023. doi: 10.5281/ZENODO.8409647.
- Johnson, K. M. and Segall, P. Viscoelastic earthquake cycle models with deep stress-driven creep along the San Andreas fault system. *Journal of Geophysical Research: Solid Earth*, 109(B10), Oct. 2004. doi: 10.1029/2004jb003096.
- Kato, N. Seismic cycle on a strike-slip fault with rate- and state-dependent strength in an elastic layer overlying a viscoelastic half-space. *Earth, Planets and Space*, 54(11):1077–1083, June 2002. doi: 10.1186/bf03353305.
- Kato, N. Complexity in the Earthquake Cycle Increases with the Number of Interacting Patches. *Pure and Applied Geophysics*, 177(10):4657–4676, July 2020. doi: 10.1007/s00024-020-02555-4.
- King, G., Stein, R., and Lin, J. Static stress changes and the triggering of earthquakes. *Bulletin of the Seismological Society of America*, 84(3):935–953, 1994. doi: 10.1785/BSSA0840030935.
- Kohli, A., Wolfson-Schwehr, M., Prigent, C., and Warren, J. M. Oceanic transform fault seismicity and slip mode influenced by seawater infiltration. *Nature Geoscience*, 14(8):606–611, Aug. 2021. doi: 10.1038/s41561-021-00778-1.
- Kohli, A. H. and Warren, J. M. Evidence for a Deep Hydrologic Cycle on Oceanic Transform Faults. *Journal of Geophysical Research: Solid Earth*, 125(2), Feb. 2020. doi: 10.1029/2019jb017751.
- Lambert, V. and Barbot, S. Contribution of viscoelastic flow in earthquake cycles within the lithosphere-asthenosphere system. *Geophysical Research Letters*, 43(19), Oct. 2016. doi: 10.1002/2016gl070345.
- Lange, D., Kopp, H., Royer, J.-Y., Henry, P., Çakir, Z., Petersen, F., Sakic, P., Ballu, V., Bialas, J., Özeren, M. S., Ergintav, S., and Géli, L. Interseismic strain build-up on the submarine North Anatolian Fault offshore Istanbul. *Nature Communications*, 10(1), July 2019. doi: 10.1038/s41467-019-11016-z.
- Li, S., Grapenthin, R., Sigmundsson, F., Drouin, V., Hreinsdóttir, S., and Ófeigsson, B. G. Post-rifting relaxation during 2015–2020 following the Bárðarbunga-Holuhraun dike intrusion and eruption in Iceland. *Geophysical Research Letters*, 49(13), July 2022. doi: 10.1029/2022gl098977.
- Liu, T., Gong, J., Fan, W., and Lin, G. In-Situ Vp/Vs Reveals Fault-Zone Material Variation at the Westernmost Gofar Transform Fault, East Pacific Rise. *Journal of Geophysical Research: Solid Earth*, 128(3), Mar. 2023. doi: 10.1029/2022jb025310.
- Liu, Y., McGuire, J. J., and Behn, M. D. Aseismic transient slip on the Gofar transform fault, East Pacific Rise. *Proceedings of the National Academy of Sciences*, 117(19):10188–10194, Apr. 2020. doi: 10.1073/pnas.1913625117.
- Lowry, A. R., Ribe, N. M., and Smith, R. B. Dynamic elevation of the Cordillera, western United States. *Journal of Geophysical Research: Solid Earth*, 105(B10):23371–23390, Oct. 2000. doi: 10.1029/2000jb900182.
- Lu, Z., Audet, P., Li, C., Zhu, S., and Wu, Z. What Controls Effective Elastic Thickness of the Lithosphere in the Pacific Ocean? *Journal of Geophysical Research: Solid Earth*, 126(3), Mar. 2021. doi: 10.1029/2020jb021074.
- Lynch, J., Burgmann, R., and Richards, M. When faults communicate: Viscoelastic coupling and earthquake clustering in a simple two-fault system. *Geophysical Research Letters*, 30(6), Mar. 2003. doi: 10.1029/2002gl016765.
- McGuire, J. J. Seismic Cycles and Earthquake Predictability on East Pacific Rise Transform Faults. *Bulletin of the Seismological Society of America*, 98(3):1067–1084, June 2008. doi: 10.1785/0120070154.
- McGuire, J. J. and Collins, J. A. Millimeter-level precision in a seafloor geodesy experiment at the Discovery transform fault, East Pacific Rise. *Geochemistry, Geophysics, Geosystems*, 14(10): 4392–4402, Oct. 2013. doi: 10.1002/ggge.20225.
- McGuire, J. J., Collins, J. A., Gouédard, P., Roland, E., Lizarralde, D., Boettcher, M. S., Behn, M. D., and van der Hilst, R. D. Variations in earthquake rupture properties along the Gofar transform fault, East Pacific Rise. *Nature Geoscience*, 5(5):336–341, Apr. 2012. doi: 10.1038/ngeo1454.
- Mildon, Z. K., Roberts, G. P., Faure Walker, J. P., and Toda, S. Coulomb pre-stress and fault bends are ignored yet vital factors for earthquake triggering and hazard. *Nature Communications*, 10(1), June 2019. doi: 10.1038/s41467-019-10520-6.
- Nishimura, C. E. and Forsyth, D. W. Rayleigh wave phase velocities in the Pacific with implications for azimuthal anisotropy and lateral heterogeneities. *Geophysical Journal International*, 94(3): 479–501, Sept. 1988. doi: 10.1111/j.1365-246x.1988.tb02270.x.
- Pan, J., Antolik, M., and Dziewonski, A. M. Locations of mid-oceanic earthquakes constrained by seafloor bathymetry. *Journal of Geophysical Research: Solid Earth*, 107(B11), Nov. 2002. doi: 10.1029/2001jb001588.
- Philibosian, B. and Meltzner, A. J. Segmentation and supercycles: A catalog of earthquake rupture patterns from the Sumatran Sunda Megathrust and other well-studied faults worldwide. *Quaternary Science Reviews*, 241:106390, Aug. 2020. doi: 10.1016/j.quascirev.2020.106390.
- Pockalny, R. A. Evidence of transpression along the Clipperton Transform: Implications for processes of plate boundary reorganization. *Earth and Planetary Science Letters*, 146(3–4): 449–464, Feb. 1997. doi: 10.1016/s0012-821x(96)00253-1.
- Pollitz, F. F. Lithosphere and shallow asthenosphere rheology from observations of post-earthquake relaxation. *Physics of the Earth and Planetary Interiors*, 293:106271, Aug. 2019. doi: 10.1016/j.pepi.2019.106271.
- Pollitz, F. F., Wicks, C., and Thatcher, W. Mantle Flow Beneath a Continental Strike-Slip Fault: Postseismic Deformation After the 1999 Hector Mine Earthquake. *Science*, 293(5536):1814–1818, Sept. 2001. doi: 10.1126/science.1061361.
- Pollitz, F. F., Wicks, C. W., Svarc, J. L., Phillips, E., Brooks, B. A., Murray, M. H., and Turner, R. C. Postseismic Relaxation Following the 2019 Ridgecrest, California, Earthquake Sequence. *Bulletin of the Seismological Society of America*, 112(2):734–749, Dec. 2021. doi: 10.1785/0120210170.
- Roland, E., Behn, M. D., and Hirth, G. Thermal-mechanical behav-

- ior of oceanic transform faults: Implications for the spatial distribution of seismicity. *Geochemistry, Geophysics, Geosystems*, 11(7), July 2010. doi: 10.1029/2010gc003034.
- Roland, E., Lizarralde, D., McGuire, J. J., and Collins, J. A. Seismic velocity constraints on the material properties that control earthquake behavior at the Quebrada-Discovery-Gofar transform faults, East Pacific Rise. *Journal of Geophysical Research: Solid Earth*, 117(B11), Nov. 2012. doi: 10.1029/2012jb009422.
- Rubinstein, J. L., Ellsworth, W. L., Chen, K. H., and Uchida, N. Fixed recurrence and slip models better predict earthquake behavior than the time- and slip-predictable models: 1. Repeating earthquakes. *Journal of Geophysical Research: Solid Earth*, 117(B2), Feb. 2012. doi: 10.1029/2011jb008724.
- Ryan, W. B. F., Carbotte, S. M., Coplan, J. O., O'Hara, S., Melkonian, A., Arko, R., Weissel, R. A., Ferrini, V., Goodwillie, A., Nitsche, F., Bonczkowski, J., and Zemsky, R. Global Multi-Resolution Topography synthesis. *Geochemistry, Geophysics, Geosystems*, 10(3), 2009. doi: <https://doi.org/10.1029/2008GC002332>.
- Sandwell, D. and Smith-Konter, B. Maxwell: A semi-analytic 4D code for earthquake cycle modeling of transform fault systems. *Computers and Geosciences*, 114:84–97, May 2018. doi: 10.1016/j.cageo.2018.01.009.
- Savage, J. C. and Burford, R. O. Geodetic determination of relative plate motion in central California. *Journal of Geophysical Research*, 78(5):832–845, Feb. 1973. doi: 10.1029/jb078i005p00832.
- Scholz, C. H. *The Mechanics of Earthquakes and Faulting*. Cambridge University Press, May 2002. doi: 10.1017/cbo9780511818516.
- Shan, B., Xiong, X., Wang, R., Zheng, Y., and Yang, S. Coulomb stress evolution along Xianshuihe–Xiaojiang Fault System since 1713 and its interaction with Wenchuan earthquake, May 12, 2008. *Earth and Planetary Science Letters*, 377–378:199–210, Sept. 2013. doi: 10.1016/j.epsl.2013.06.044.
- Shi, P., Wei, M., and Barbot, S. Contribution of Viscoelastic Stress to the Synchronization of Earthquake Cycles on Oceanic Transform Faults. *Journal of Geophysical Research: Solid Earth*, 127(8), Aug. 2022. doi: 10.1029/2022jb024069.
- Shimazaki, K. and Nakata, T. Time-predictable recurrence model for large earthquakes. *Geophysical Research Letters*, 7(4): 279–282, Apr. 1980. doi: 10.1029/gl007i004p00279.
- Smith, B. and Sandwell, D. Coulomb stress accumulation along the San Andreas Fault system. *Journal of Geophysical Research: Solid Earth*, 108(B6), June 2003. doi: 10.1029/2002jb002136.
- Smith, B. and Sandwell, D. A three-dimensional semianalytic viscoelastic model for time-dependent analyses of the earthquake cycle. *Journal of Geophysical Research: Solid Earth*, 109(B12), Dec. 2004. doi: 10.1029/2004jb003185.
- Smith, B. R. and Sandwell, D. T. A model of the earthquake cycle along the San Andreas Fault System for the past 1000 years. *Journal of Geophysical Research: Solid Earth*, 111(B1), Jan. 2006. doi: 10.1029/2005jb003703.
- Smith-Konter, B. R., Sandwell, D. T., and Shearer, P. Locking depths estimated from geodesy and seismology along the San Andreas Fault System: Implications for seismic moment release. *Journal of Geophysical Research*, 116(B6), June 2011. doi: 10.1029/2010jb008117.
- Smith-Konter, B. R., Thornton, G. M., and Sandwell, D. T. Vertical crustal displacement due to interseismic deformation along the San Andreas fault: Constraints from tide gauges. *Geophysical Research Letters*, 41(11):3793–3801, June 2014. doi: 10.1002/2014gl060091.
- Smith-Konter, B. and Sandwell, D. Stress evolution of the San Andreas fault system: Recurrence interval versus locking depth. *Geophysical Research Letters*, 36(13), July 2009. doi: 10.1029/2009gl037235.
- Stein, R. S., Barka, A. A., and Dieterich, J. H. Progressive failure on the North Anatolian fault since 1939 by earthquake stress triggering. *Geophysical Journal International*, 128(3):594–604, Mar. 1997. doi: 10.1111/j.1365-246x.1997.tb05321.x.
- Sykes, L. R. and Ekström, G. Earthquakes along Eltanin transform system, SE Pacific Ocean: Fault segments characterized by strong and poor seismic coupling and implications for long-term earthquake prediction. *Geophysical Journal International*, 188(2):421–434, Dec. 2011. doi: 10.1111/j.1365-246x.2011.05284.x.
- Ward, L. A., Smith-Konter, B. R., Xu, X., and Sandwell, D. T. Seismic Moment Accumulation Response to Lateral Crustal Variations of the San Andreas Fault System. *Journal of Geophysical Research: Solid Earth*, 126(4), Apr. 2021. doi: 10.1029/2020jb021208.
- Ward, L. A., Guns, K. A., Smith-Konter, B. R., Xu, X., Bock, Y., and Sandwell, D. T. Vertical Postseismic Deformation of the 2019 Ridgecrest Earthquake Sequence. *Journal of Geophysical Research: Solid Earth*, 127(6), June 2022. doi: 10.1029/2021jb023331.
- Watts, A. and Burov, E. Lithospheric strength and its relationship to the elastic and seismogenic layer thickness. *Earth and Planetary Science Letters*, 213(1–2):113–131, Aug. 2003. doi: 10.1016/s0012-821x(03)00289-9.
- Watts, A. B. An analysis of isostasy in the world's oceans; 1. Hawaiian-Emperor Seamount Chain. *Journal of Geophysical Research: Solid Earth*, 83(B12):5989–6004, Dec. 1978. doi: 10.1029/jb083ib12p05989.
- Watts, A. B. and Zhong, S. Observations of flexure and the rheology of oceanic lithosphere. *Geophysical Journal International*, 142(3):855–875, Sept. 2000. doi: 10.1046/j.1365-246x.2000.00189.x.
- Watts, D. R., Wei, M., Tracey, K. L., Donohue, K. A., and He, B. Seafloor Geodetic Pressure Measurements to Detect Shallow Slow Slip Events: Methods to Remove Contributions From Ocean Water. *Journal of Geophysical Research: Solid Earth*, 126(4), Apr. 2021. doi: 10.1029/2020jb020065.
- Wei, M. and Shi, P. Synchronization of Earthquake Cycles of Adjacent Segments on Oceanic Transform Faults Revealed by Numerical Simulation in the Framework of Rate-and-State Friction. *Journal of Geophysical Research: Solid Earth*, 126(1), Jan. 2021. doi: 10.1029/2020jb020231.
- Weldon, R. J., Fumal, T. E., Biasi, G. P., and Scharer, K. M. Past and Future Earthquakes on the San Andreas Fault. *Science*, 308(5724):966–967, May 2005. doi: 10.1126/science.1111707.
- Wells, D. L. and Coppersmith, K. J. New empirical relationships among magnitude, rupture length, rupture width, rupture area, and surface displacement. *Bulletin of the Seismological Society of America*, 84(4):974–1002, Aug. 1994. doi: 10.1785/bssa0840040974.
- Wessel, P., Luis, J. F., Uieda, L., Scharroo, R., Wobbe, F., Smith, W. H. F., and Tian, D. The Generic Mapping Tools Version 6. *Geochemistry, Geophysics, Geosystems*, 20(11):5556–5564, 2019. doi: <https://doi.org/10.1029/2019GC008515>.
- Wolfson-Schwehr, M. and Boettcher, M. S. *Global Characteristics of Oceanic Transform Fault Structure and Seismicity*, page 21–59. Elsevier, 2019. doi: 10.1016/b978-0-12-812064-4.00002-5.
- Wolfson-Schwehr, M., Boettcher, M. S., McGuire, J. J., and Collins, J. A. The relationship between seismicity and fault structure on the Discovery transform fault, East Pacific Rise. *Geochemistry, Geophysics, Geosystems*, 15(9):3698–3712, Sept. 2014. doi: 10.1002/2014gc005445.

Yamamoto, R., Kido, M., Ohta, Y., Takahashi, N., Yamamoto, Y., Pinar, A., Kalafat, D., Özener, H., and Kaneda, Y. Seafloor Geodesy Revealed Partial Creep of the North Anatolian Fault Submerged in the Sea of Marmara. *Geophysical Research Letters*, 46(3):1268–1275, Feb. 2019. doi: 10.1029/2018gl080984.

Yao, H., Gouédard, P., Collins, J. A., McGuire, J. J., and van der Hilst, R. D. Structure of young East Pacific Rise lithosphere from ambient noise correlation analysis of fundamental- and higher-mode Scholte-Rayleigh waves. *Comptes Rendus. Géoscience*, 343(8–9):571–583, June 2011. doi: 10.1016/j.crte.2011.04.004.

The article *A model of the earthquake cycle along the Gofar oceanic transform faults* © 2024 by Meng (Matt) Wei is licensed under CC BY 4.0.